A&A, 708, A272 (2026)
https://doi.org/10.1051/0004-6361/202556348

Astronomy & Astrophysics

TOI-1259Ab: A warm Jupiter orbiting a K-dwarf white-dwarf binary on a low-obliquity orbit

Hugo Veldhuis[1,⋆], Juan I. Espinoza-Retamal[1,2,3,4], Gudmundur Stefansson[1], Alexander P. Stephan[5], David V. Martin[5], David Bruijne[1], Suvrath Mahadevan[7,8], Joshua N. Winn[4], Cullen H. Blake[9], Fei Dai[10], Rachel B. Fernandes[6,7,⋆⋆], Evan Fitzmaurice[7,8,11], Eric B. Ford[7,8,11,12], Mark R. Giovinazzi[13], Arvind F. Gupta[14], Samuel Halverson[15], Te Han[16], Daniel Krolikowski[17], Joe Ninan[18], Cristobal Petrovich[19], Paul Robertson[16], Arpita Roy[20], Christian Schwab[21], and Ryan Terrien[22]

[1] Anton Pannekoek Institute for Astronomy, University of Amsterdam, Science Park 904, 1098 XH Amsterdam, The Netherlands
[2] Instituto de Astrofísica, Pontificia Universidad Católica de Chile, Av. Vicuña Mackenna 4860, 782-0436 Macul, Santiago, Chile
[3] Millennium Institute for Astrophysics, Santiago, Chile
[4] Department of Astrophysical Sciences, Princeton University, 4 Ivy Lane, Princeton, NJ 08544, USA
[5] Department of Physics and Astronomy, Vanderbilt University, TN 37235, USA
[6] Department of Physics and Astronomy, Tufts University, 574 Boston Avenue, Medford, MA 02155, USA
[7] Department of Astronomy & Astrophysics, The Pennsylvania State University, 525 Davey Laboratory, University Park, PA 16802, USA
[8] Center for Exoplanets and Habitable Worlds, The Pennsylvania State University, 525 Davey Laboratory, University Park, PA 16802, USA
[9] Department of Physics and Astronomy, University of Pennsylvania, 209 South 33rd Street, Philadelphia, PA 19104, USA
[10] Institute for Astronomy, University of Hawai'i, 2680 Woodlawn Drive, Honolulu, HI 96822, USA
[11] Institute for Computational and Data Sciences, The Pennsylvania State University, University Park, PA 16802, USA
[12] Center for Astrostatistics, 525 Davey Laboratory, The Pennsylvania State University, University Park, PA 16802, USA
[13] Department of Physics and Astronomy, Amherst College, Amherst, MA 01002, USA
[14] U.S. National Science Foundation National Optical-Infrared Astronomy Research Laboratory, 950 N. Cherry Ave., Tucson, AZ 85719, USA
[15] Jet Propulsion Laboratory, California Institute of Technology, 4800 Oak Grove Drive, Pasadena, CA 91109, USA
[16] Department of Physics & Astronomy, The University of California, Irvine, Irvine, CA 92697, USA
[17] Steward Observatory, University of Arizona, 933 N. Cherry Ave, Tucson, AZ 85721, USA
[18] Department of Astronomy and Astrophysics, Tata Institute of Fundamental Research, Homi Bhabha Road, Colaba, Mumbai 400005, India
[19] Department of Astronomy, Indiana University, Bloomington, IN 47405, USA
[20] Astrophysics & Space Institute, Schmidt Sciences, New York, NY 10011, USA
[21] School of Mathematical and Physical Sciences, Macquarie University, Balaclava Road, North Ryde, NSW 2109, Australia
[22] Carleton College, One North College Street, Northfield, MN 55057, USA

Received 10 July 2025 / Accepted 23 December 2025

ABSTRACT

The evolution of one member of a stellar binary into a white dwarf has been proposed as a mechanism that triggers the formation of close-in gas giant planets. The star's asymmetric mass loss during the Asymptotic Giant Branch stage gives it a velocity recoil or "kick" that can initiate eccentric Lidov–Kozai oscillations, potentially causing a planet around the secondary star to migrate inward and perturb the eccentricity and inclination of its orbit. Here we present a measurement of the stellar obliquity of TOI-1259Ab, a gas giant in a close-in orbit around a K star with a white dwarf companion about 1650 au away. By using the NEID spectrograph to detect the Rossiter-McLaughlin effect during the planetary transit, we find the sky-projected obliquity to be $\lambda = \mathbf{7}^{+\mathbf{20}}_{-\mathbf{21}}{}^{\circ}$. When combined with estimates of the stellar rotation period, radius, and projected rotation velocity, we find the true 3D obliquity to be $\psi = 24^{+14}_{-12}{}^{\circ}$ ($\psi < \mathbf{47}^{\circ}$ at 95% confidence), revealing that the orbit of TOI-1259Ab is on a low-obliquity orbit with respect to the star's equatorial plane. Because the planet's orbit is too wide for tidal realignment to be expected, TOI-1259Ab might have formed quiescently in this low-obliquity configuration. Alternatively, as we show with dynamical simulations, eccentric Lidov–Kozai oscillations triggered by the evolution of the binary companion expect to lead to a low-obliquity configuration with a probability of ∼14%.

Key words. techniques: radial velocities – planets and satellites: dynamical evolution and stability – planets and satellites: gaseous planets – planets and satellites: individual: TOI-1259Ab – binaries: general – white dwarfs

⋆ Corresponding author: hugoveldhuis1@gmail.com
⋆⋆ President's Postdoctoral Fellow.

1. Introduction

Since the discovery of the first exoplanet around a solar-type star (Mayor & Queloz 1995), the existence of gas giants in short-period orbits has been puzzling. The theories proposed to explain these close-in planets typically fall into three categories (see, e.g., Dawson & Johnson 2018). The first category is high-eccentricity migration, where a planet that formed beyond the ice line of the protoplanetary disk is launched onto a highly eccentric orbit through planet–planet scattering (e.g., Rasio & Ford 1996; Beaugé & Nesvorný 2012), eccentric Lidov–Kozai (ELK) oscillations (e.g., Kozai 1962; Lidov 1962; Naoz 2016), or other secular interactions (e.g., Wu & Lithwick 2011; Petrovich 2015), after which tidal friction circularizes and shrinks the orbit. The second category is disk-driven migration, where the planet spirals inward as a consequence of gravitational tidal interactions with the gaseous protoplanetary disk (e.g., Goldreich & Tremaine 1980; Lin & Papaloizou 1986). The third category is in situ formation, where the planet forms close to the star, despite prior theoretical arguments against it (e.g., Batygin et al. 2016; Boley et al. 2016).

Insights into the formation and evolution of planetary systems can be gained from studying the stellar obliquity (ψ) – the angle between a star's spin axis and the planet's orbital axis (see, e.g., Albrecht et al. 2022). For the planets in the Solar System, these angles are low, with a ∼7° inclination of the solar rotation axis as seen from Earth (Beck & Giles 2005). In contrast, observations of the Rossiter-McLaughlin (RM) effect (McLaughlin 1924; Rossiter 1924) have revealed a wide range of obliquities seen in exoplanet systems, including well-aligned, polar, and even retrograde orbits. Recently, Albrecht et al. (2021) found hints of a preponderance of nearly polar orbits in the obliquity distribution of exoplanet systems, which subsequent studies have confirmed and connected to specific types of exoplanets (see, e.g., Siegel et al. 2023; Dong & Foreman-Mackey 2023; Espinoza-Retamal et al. 2024; Attia et al. 2023; Bourrier et al. 2023).

Recent work by Stephan et al. (2024) suggests that the evolution to the white dwarf (WD) phase of a stellar companion can increase the probability of high-eccentricity migration of gas giant planets. The star's asymmetric mass loss during the asymptotic giant branch phase induces a velocity recoil, often called a "kick" (e.g., Fregeau et al. 2009; El-Badry & Rix 2018). This kick could cause the orbit of the companion to tilt with respect to the orbital plane of the planet, a condition that allows for ELK oscillations (e.g., Wu & Murray 2003; Fabrycky & Tremaine 2007; Naoz et al. 2012). This formation scenario could be tested with a population of obliquity measurements of systems with a WD companion. This population, however, remains quite meager, as only three obliquity measurements of such systems have been reported (Esposito et al. 2014; Smith et al. 2013; Brown et al. 2017; Zak et al. 2025). Furthermore, at the time of the obliquity measurement, two of their WD companions had not been detected, so their novel architectures had not been discussed.

Here, we present a measurement of a low obliquity for TOI-1259Ab, a close-in gas giant orbiting a bright K star with a WD companion (Martin et al. 2021; Fitzmaurice et al. 2022). We detected the RM effect using precise radial velocity (RV) observations with the NEID spectrograph on the WIYN[1] 3.5 m telescope at Kitt Peak in Arizona. Having a relatively large orbital separation ($a/R_\star \approx 12$; Martin et al. 2021), the planet's orbit is too wide for tidal realignment to be expected, making it seem likely that the system formed with a low obliquity. To further investigate the WD-kick formation scenario proposed by Stephan et al. (2024), we performed ELK simulations of the system and compared the measured obliquity value of TOI-1259Ab with the distribution of the obliquities predicted by the simulations.

This paper is structured as follows. In Section 2, we present the TOI-1259 system, and we discuss the observations in Section 3. In Section 4, we discuss our analysis of the RM effect of TOI-1259Ab and its accompanying datasets. In Section 5, we put our results in context with previous obliquity measurements, and we show that a low obliquity is a possible but somewhat improbable outcome of the WD kick formation scenario. We conclude with a summary of our findings in Section 6.

2. The TOI-1259 system

TOI-1259 is a binary system, consisting of a $0.744^{+0.064}_{-0.059}\,M_\odot$ K-dwarf primary star ($T_{\rm eff}$ = 4775 ± 100 K) and a 0.561 ± 0.021 $M_\odot$ WD companion (Martin et al. 2021). Using data from the Transiting Exoplanet Survey Satellite (TESS; Ricker et al. 2015), combined with RV follow-up observations, Martin et al. (2021) discovered a transiting close-in gas giant around the primary star, with an orbital period of $P = 3.4779780^{+0.0000019}_{-0.0000017}$ days, a mass of $M_p = 0.441^{+0.049}_{-0.047}\,M_J$, and a radius of $R_p = 1.022^{+0.030}_{-0.027}\,R_J$. Recent work by Saidel et al. (2025) found evidence for an extended escaping atmosphere of the planet but concluded that atmospheric mass loss has not significantly altered the properties of the planet.

Martin et al. (2021) derived the age of the TOI-1259 system using two independent methods. First, the TESS light curves reveal photometric modulation of TOI-1259A with a period of ∼28 days. Using the TESS-systematics-insensitive periodogram (TESS-SIP; Hedges et al. 2020), this was determined to be likely the stellar rotation period rather than TESS systematics. Using gyrochronology, the age of TOI-1259A was calculated to be $4.8^{+0.7}_{-0.8}$ Gyr. Second, since WDs steadily cool over time, a measurement of the effective temperature serves as a proxy for the WD's age. From WD cooling, Martin et al. (2021) determined that TOI-1259B's age was roughly consistent with that of TOI-1259A, as expected for a coeval binary: ≈3.5–6.37, depending on assumptions about the WD atmosphere and the initial-final mass relation.

Follow-up spectroscopy of the WD by Fitzmaurice et al. (2022) revealed it to be a DA-type WD, characterized by strong hydrogen Balmer absorption lines as its only prominent spectral features (see, e.g., Saumon et al. 2022). This classification allowed for tighter constraints by WD cooling models, constraining the age of TOI-1259B to $4.0^{+1.0}_{-0.4}$ Gyr. TOI-1259B shows no signs of atmospheric pollution by heavy elements. Such pollution is observed in approximately 25–50% of WDs (e.g., Zuckerman et al. 2010; Zuckerman 2014; Koester et al. 2014) and is thought to trace the accretion of planetary debris (e.g., Aguilera-Gómez et al. 2025). However, the absence of pollution does not preclude past or present planets around TOI-1259B. For example, WD 1856+534 hosts a transiting giant planet yet shows no detectable metal lines in its spectrum (Vanderburg et al. 2020).

[1] The WIYN Observatory is a joint facility of the NSF's National Optical-Infrared Astronomy Research Laboratory, Indiana University, the University of Wisconsin-Madison, Pennsylvania State University, Purdue University, and Princeton University.

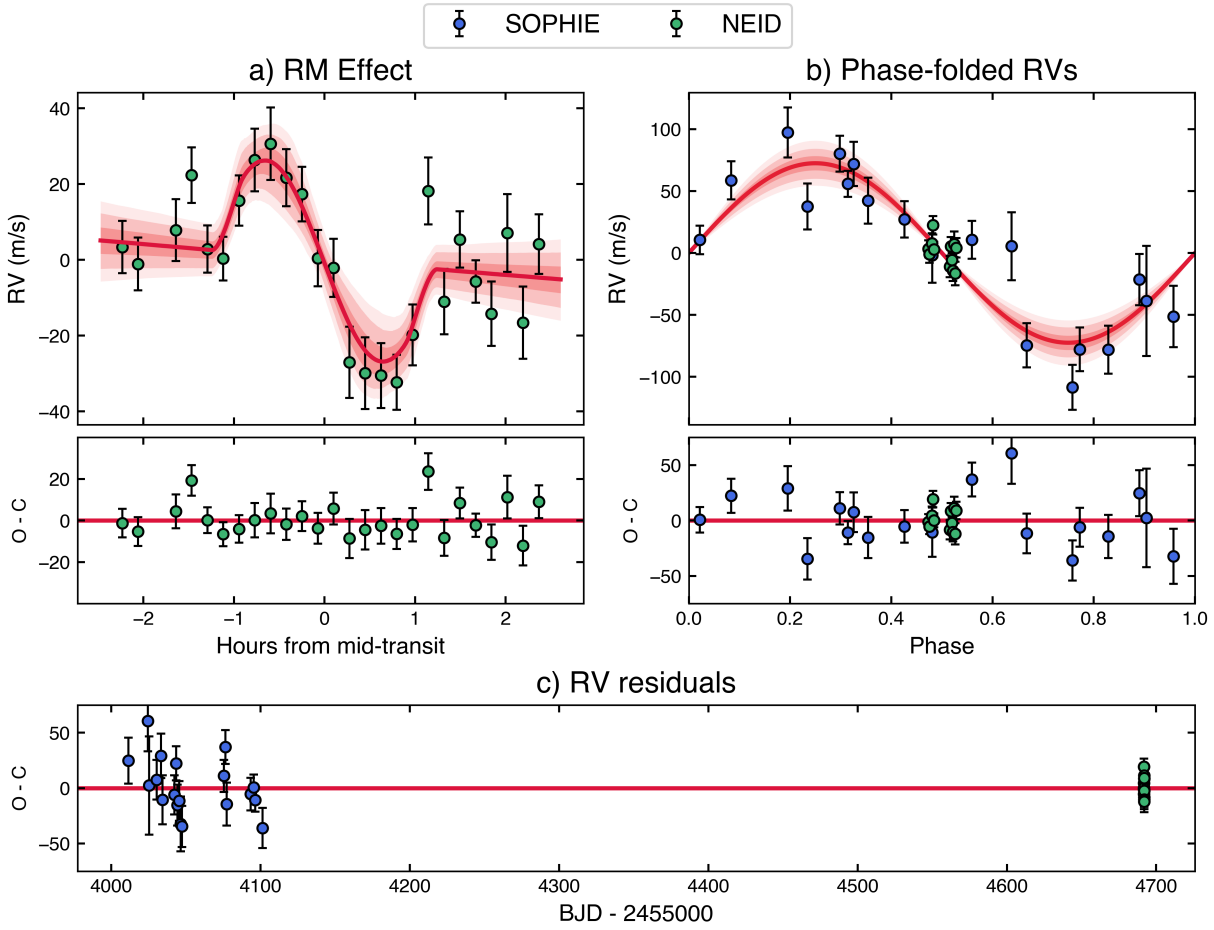

Fig. 1. Spectroscopic observations of TOI-1259A. (a) NEID observations (in green) of the RM effect produced during the transit of TOI-1259Ab, along with the best-fit model in red. Residuals are shown below. (b) Phase-folded observations from SOPHIE (in blue), as well as out-of-transit NEID data of TOI-1259Ab, with the best-fit model in red and the residuals below. (c) Residuals of all the RV data and best-fit model over observation time.

3. Observations

3.1. Spectroscopic data

We observed one transit of TOI-1259Ab using the NEID spectrograph (Schwab et al. 2016) on the WIYN 3.5 m telescope at Kitt Peak Observatory in Arizona. NEID is an environmentally stabilized (Stefansson et al. 2016; Robertson et al. 2019), high-resolution ($R \approx 110\,000$) spectrograph covering a broad wavelength range, from 3800 to 9300 Å. We observed the transit on the night of April 22, 2022, between 05:50 and 10:26 UTC. During the observation, the target rose from air mass 1.99 to 1.51. We obtained 26 spectra of the host star during the transit, each with an exposure time of 600 seconds. Observations were reduced using the NEID Data Reduction Pipeline[2] (DRP; version 1.40), and RVs were extracted using the `NEID-SERVAL` code, a spectral-matching code that builds on the SpEctrum Radial Velocity AnaLyzer (SERVAL; Zechmeister et al. 2018) code and has been adapted for NEID data (Stefànsson et al. 2022). The average signal-to-noise ratio of the final spectra in NEID order index 102 (865 nm) is 8.7 per 1D-extracted pixel, leading to an average RV precision of ~8 m s^{-1}. We see no correlation between the derived RVs and the Hα, Na D I, or Na D II stellar activity indices provided by the DRP. The extracted RVs are shown in Figure 1 and can be found in Appendix A.

[2] https://neid.ipac.caltech.edu/docs/NEID-DRP/

To better constrain the parameters of the planet and its orbit, we also used 19 archival RV observations taken with the SOPHIE spectrograph (Perruchot et al. 2008). SOPHIE is a fiber-fed high-resolution ($R \approx 75\,000$) échelle spectrograph mounted on the 1.93 m telescope of Observatoire de Haute-Provence in France. These earlier observations were used to confirm the planetary nature of the transiting object (Martin et al. 2021) and were performed between June and July 2020.

3.2. Photometric data

We analyzed the spectroscopic data in combination with photometric observations. In particular, we included the 2-minute TESS light curves from a total of 30 sectors – namely Sectors 14, 17–21, 24–26, 40, 41, 47, 48, 50–55, 58–60, 73–75, and 77–81 – produced with the TESS Science Processing Operations Center (SPOC) pipeline (Jenkins et al. 2016). This collection includes 21 more sectors than the analysis by Martin et al. (2021). We searched for, downloaded, and combined all the light curves using the `lightkurve` package (Lightkurve Collaboration 2018). Additionally, we detrended the light curve using a Matern-3/2 Gaussian process (GP) with the `juliet` (Espinoza et al. 2019) code, which uses `celerite` (Foreman-Mackey et al. 2017) for the GP and `batman` (Kreidberg 2015) to model the transits. From the `juliet` analysis, we obtained the detrended light curve and the ephemerides of the

planet, both of which were used in the final joint fit discussed in Section 4. The propagated error on the transit timing of the NEID observation using these modeled values is 11 seconds.

4. Joint analysis

To derive the parameters of the planet and its orbit, we jointly modeled all the observations described in Section 3 using the publicly accessible `ironman`[3] package (Espinoza-Retamal et al. 2024). To model transit light curves, `ironman` employs `batman` (Kreidberg 2015). To model RVs, `ironman` uses `rmfit` (Stefànsson et al. 2020; Stefànsson et al. 2022), which utilizes `radvel` (Fulton et al. 2018) to model the Keplerian orbit and the equations derived by Hirano et al. (2010) for the RM effect. `ironman` jointly fits the data using a Bayesian approach, employing dynamic nested sampling with the `dynesty` package (Speagle 2020) to sample the posteriors. To derive the stellar inclination angle, we followed Stefànsson et al. (2022) and used the λ, $\cos i_\star$, $P_{\rm rot}$, and $R_\star$ parameterization of the RM effect available within `ironman`. This correctly accounts for the correlations between $v \sin i_\star$ and the equatorial velocity of the star (see Masuda & Winn 2020). By sampling the posteriors for the stellar inclination ($\cos i_\star$), radius ($R_\star$), and rotation period (P_{rot}), the projected rotational velocity ($v \sin i_\star$) is calculated to model the RM effect, and ψ is derived at the end of the sampling as

$$\cos\psi = \cos i_\star \cos i + \sin i_\star \sin i \cos\lambda. \quad (1)$$

We placed informative Gaussian priors on the stellar mass, radius, rotational period, and the planet's orbital period based on the results of Martin et al. (2021). For almost all the remaining parameters, we placed uniform priors, except for the orbital period and time of mid-transit, which were precisely constrained in Section 3.2. In addition, for the "intrinsic stellar line width" parameter β of the RM model, which represents both instrumental broadening and macro-turbulence, we followed Stefànsson et al. (2022), assuming an instrumental broadening term of 2.5 km s^{-1} based on the resolution of NEID and adopting a macro-turbulent velocity of 2.5 km s^{-1} based on the relationships from Valenti & Fischer (2005) for $T_{\rm eff}$ = 4775 K. We added the instrumental and macro-turbulent broadening in quadrature and set this as our prior for β, with an uncertainty of 2 km s^{-1}. Finally, we also allowed for an extra RV slope in the NEID RVs to account for possible stellar activity during the transit. The list of priors and resulting posteriors is shown in Table 1.

Figure 1 shows the results from the joint `ironman` fit for both the in-transit RM effect (Figure 1a) and the out-of-transit RVs (Figure 1b). The jointly-fitted TESS photometric data, along with the best model, are shown in Figure 2. The in-transit RVs show a clear RM effect signature of a prograde orbit, shifting toward positive RV (redshifted) before reversing to negative (blueshifted). From the fit, we find that TOI-1259Ab has a low-obliquity orbit, with a sky-projected obliquity of $\lambda = \mathbf{7}^{+\mathbf{20}}_{-\mathbf{21}}{}^\circ$ and a true 3D obliquity of $\psi = 24^{+14}_{-12}{}^\circ$. The remaining best-fit parameter values listed in Table 1 are in good agreement (within 1–2σ in all cases) with the parameters reported by Martin et al. (2021).

To account for the degeneracy in ψ that exists due to the 180° degeneracy in stellar inclination, $i_\star$, we performed three different runs: a run where the $\cos i_\star$ prior ranges from 0 to 1; a run where $\cos i_\star$ ranges from –1 to 0; and a run where $\cos i_\star$ ranges from –1 to 1. This resulted in $\psi_1 = 25^{14}_{-12}$, $\psi_2 = 26^{14}_{-13}$, and $\psi_3 = 26^{15}_{-13}$, respectively, with the $\cos i_\star$ posterior centering around 0° (see Appendix B). We see that the runs are consistent and all other parameters remain the same. As such, we elected to adopt the results from the latter run. Additionally, we experimented with fitting slightly different models to the available data. We evaluated the possibility of an eccentric orbit for the planet and of a long-term quadratic or linear trend (and all combinations thereof). We elected to adopt the circular fit without any long-term trends, as the Bayesian evidence ($\log Z$) favored this model over the others we considered, with Bayes factors $\Delta \log Z > 2$ and ΔBIC > 10 compared to all the other models.

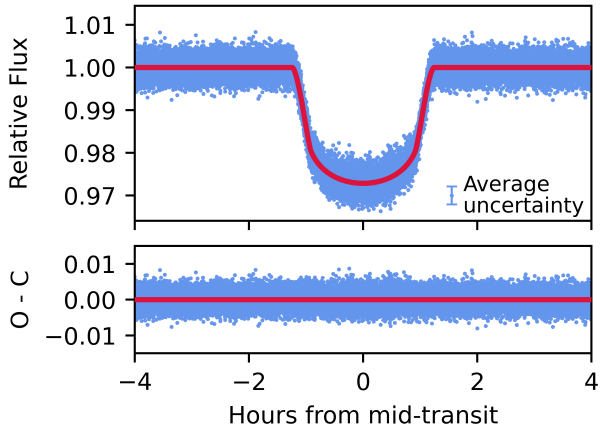

Fig. 2. Phase-folded, detrended TESS data (blue) from the 30 TESS sectors analyzed in this work, along with the best-fit transit model from the `ironman` joint-fit analysis (red line). Data points are shown without error bars; nevertheless, we show the median error of 2100 ppm. The residuals are shown in the bottom panel.

5. Discussion

5.1. TOI-1259Ab in context

Figure 3 shows the population of sky-projected (top) and 3D (bottom) obliquity measurements against the effective temperature of the planet's host star, separated into stars without known stellar companions (left) and known binaries or triples (right). The obliquities were taken from TEPCat[4] (Southworth 2011) as of May 2025. At our time of retrieval, a few published results were missing and therefore added manually: KELT-25 and KELT-26 from Martínez et al. (2020); AB Pic b, as reported by Kraus et al. (2020); TOI-451, TOI-455, and WASP-26 from Knudstrup et al. (2024); and WASP-35, WASP-44, WASP-45, WASP-54, WASP-91, WASP-99, WASP-129, WASP-162, and Qatar-7 from Zak et al. (2025). We excluded nine systems (HAT-P-27, WASP-49, CoRoT-1, CoRoT-19, HATS-14, WASP-134, WASP-23, WASP-1, and WASP-2), which Albrecht et al. (2022) considered unreliable or too uncertain, and use a more reliable measurement of 55 Cnc e recently published by Zhao et al. (2023).

We divided the sample into different types of planets using their NASA Exoplanet Archive[5] (Akeson et al. 2013; Christiansen et al. 2025) entries. We considered four categories: hot Jupiters ($0.4 < M_p/M_{\rm J} < 13$ & $a/R_\star < 11$), warm Jupiters ($0.4 < M_p/M_{\rm J} < 13$ & $a/R_\star > 11$), hot Saturns ($0.2 < M_p/M_{\rm J} < 0.4$ & $a/R_\star < 11$), and warm Saturns ($0.2 < M_p/M_{\rm J} < 0.4$ & $a/R_\star > 11$). The NASA Exoplanet Archive also distinguishes apparently single stars from known multiple-star systems.

[3] https://github.com/jiespinozar/ironman

[4] https://www.astro.keele.ac.uk/jkt/tepcat/

[5] https://exoplanetarchive.ipac.caltech.edu/index.html

Table 1. Priors and resulting posteriors from the `ironman` joint fit of available TESS photometry, NEID RM effect RVs, and out-of-transit RVs from SOPHIE.

Parameter	Description	Prior	Posterior
λ	Sky-projected stellar obliquity (°)	$\mathcal{U}(-180, 180)$	7^{+20}_{-21}
ψ	3D stellar obliquity (°)	...	24^{+14}_{-12}
$R_\star$	Stellar radius ($R_\odot$)	$\mathcal{N}(0.711, 0.020)$	0.715 ± 0.015
$M_\star$	Stellar mass ($M_\odot$)	$\mathcal{N}(0.74, 0.06)$	$0.746^{+0.048}_{-0.044}$
$P_{\rm rot,\star}$	Stellar rotational period (days)	$\mathcal{N}(28.0, 2.8)$	26.7 ± 2.8
$\cos i_\star$	Cosine of stellar inclination	$\mathcal{U}(-1, 1)$	$0.04^{+0.34}_{-0.32}$
$v_{\rm eq,\star}$	Stellar equatorial velocity (km s^{-1})	...	$1.37^{+0.17}_{-0.13}$
$v \sin i_\star$	Projected rotational velocity (km s^{-1})	...	$1.28^{+0.17}_{-0.14}$
$\rho_\star$	Stellar density (g cm^{-3})	...	$2.89^{+0.03}_{-0.04}$
$i_\star$	Stellar inclination (°)	...	92^{+19}_{-20}
$R_{\rm p}$	Planet Radius ($R_\oplus$)	...	11.6 ± 0.2
a	Semimajor axis (au)	...	0.0408 ± 0.0009
$M_{\rm p}$	Planet mass ($M_\oplus$)	...	141 ± 13
$\rho_{\rm p}$	Planet density (g cm^{-3})	...	0.49 ± 0.04
P	Orbital Period (days)	$\mathcal{N}(3.477978, 0.000002)$	3.4779792 ± 0.0000001
t_0	Transit midpoint (BJD)	$\mathcal{N}(2458686.7005, 0.0001)$	$2458686.70048 \pm 0.00004$
b	Impact parameter	$\mathcal{U}(0, 1)$	$0.10^{+0.05}_{-0.07}$
$R_{\rm p}/R_\star$	Radius ratio	$\mathcal{U}(0, 1)$	0.145 ± 0.004
e	Orbital eccentricity	Fixed	0
K	RV semiamplitude (m s^{-1})	$\mathcal{U}(0, 1000)$	72 ± 6
$a/R_\star$	Scaled semimajor axis	...	$12.27^{+0.05}_{-0.06}$
i	Orbital inclination (°)	...	$89.5^{+0.3}_{-0.2}$
$q_1^{\rm TESS}$	TESS linear limb-darkening parameter	$\mathcal{U}(0, 1)$	$0.41^{+0.03}_{-0.04}$
$q_2^{\rm TESS}$	TESS quadratic limb-darkening parameter	$\mathcal{U}(0, 1)$	$0.36^{+0.03}_{-0.03}$
$\sigma_{\rm TESS}$	TESS photometric jitter (ppm)	$\mathcal{LU}(1, 5 \times 10^7)$	$5.0^{+9.2}_{-3.3}$
$\gamma_{\rm SOPHIE}$	SOPHIE RV offset (m s^{-1})	$\mathcal{U}(-41\,000, -40\,500)$	$-40\,820 \pm 4$
$\sigma_{\rm SOPHIE}$	SOPHIE RV jitter (m s^{-1})	$\mathcal{LU}(10^{-3}$,100)	$0.5^{+12.4}_{-0.5}$
$q_1^{\rm NEID}$	NEID linear limb-darkening parameter	$\mathcal{U}(0, 1)$	$0.78^{+0.16}_{-0.27}$
$q_2^{\rm NEID}$	NEID quadratic limb-darkening parameter	$\mathcal{U}(0, 1)$	$0.66^{+0.24}_{-0.35}$
$\beta_{\rm NEID}$	Intrinsic stellar line width (km s^{-1})	$\mathcal{TN}(3.5, 2.0, 0.0, 10.0)$	$0.61^{+0.90}_{-0.37}$
$\gamma_{\rm NEID}$	NEID RV offset (m s^{-1})	$\mathcal{U}(-50, 50)$	-2.5 ± 1.6
$\sigma_{\rm NEID}$	NEID RV jitter (m s^{-1})	$\mathcal{LU}(10^{-3}, 100)$	$0.08^{+2.0}_{-0.08}$
$\dot{\gamma}_{\rm NEID}$	NEID RV slope (m s^{-1} day^{-1})	$\mathcal{U}(-200, 200)$	81 ± 31

Notes. $\mathcal{U}(a, b)$ denotes a uniform distribution between a and b. $\mathcal{N}(\mu, \sigma)$ denotes a Gaussian distribution with mean μ and standard deviation σ. $\mathcal{TN}(\mu, \sigma, a, b)$ denotes a truncated Gaussian distribution with mean μ and standard deviation σ, constrained between limits a and b. $\mathcal{LU}(a, b)$ denotes a log-uniform prior between a and b. The nested sampling jump parameters are the parameters shown with associated priors, and the remaining parameters are derived from those posteriors.

However, this is not fully up-to-date. We supplemented it by looking up the systems in four binary catalogs: the common proper-motion catalogs based on Gaia Data Release 3 (DR3) (Gaia Collaboration 2023) presented by El-Badry et al. (2021), Mugrauer & Michel (2021), and Mugrauer et al. (2022), and the direct-imaging catalog of Schlagenhauf et al. (2024).

Figure 3 shows that the obliquity distributions of hot Jupiters around both single stars and binaries appear to be similar. They both exhibit a broadening of possible obliquities at around $T_{\rm eff}$ = 6100 K, shifting from all aligned to more isotopically distributed as their hosts get hotter (Winn et al. 2010; Schlaufman 2010). This turning point is consistent with the Kraft break (Kraft 1967), below which stars have deep convective envelopes that enable more efficient tidal realignment than in hotter stars with radiative outer layers (e.g., Winn et al. 2010; Albrecht et al. 2012; Rice et al. 2022a; Zanazzi et al. 2024).

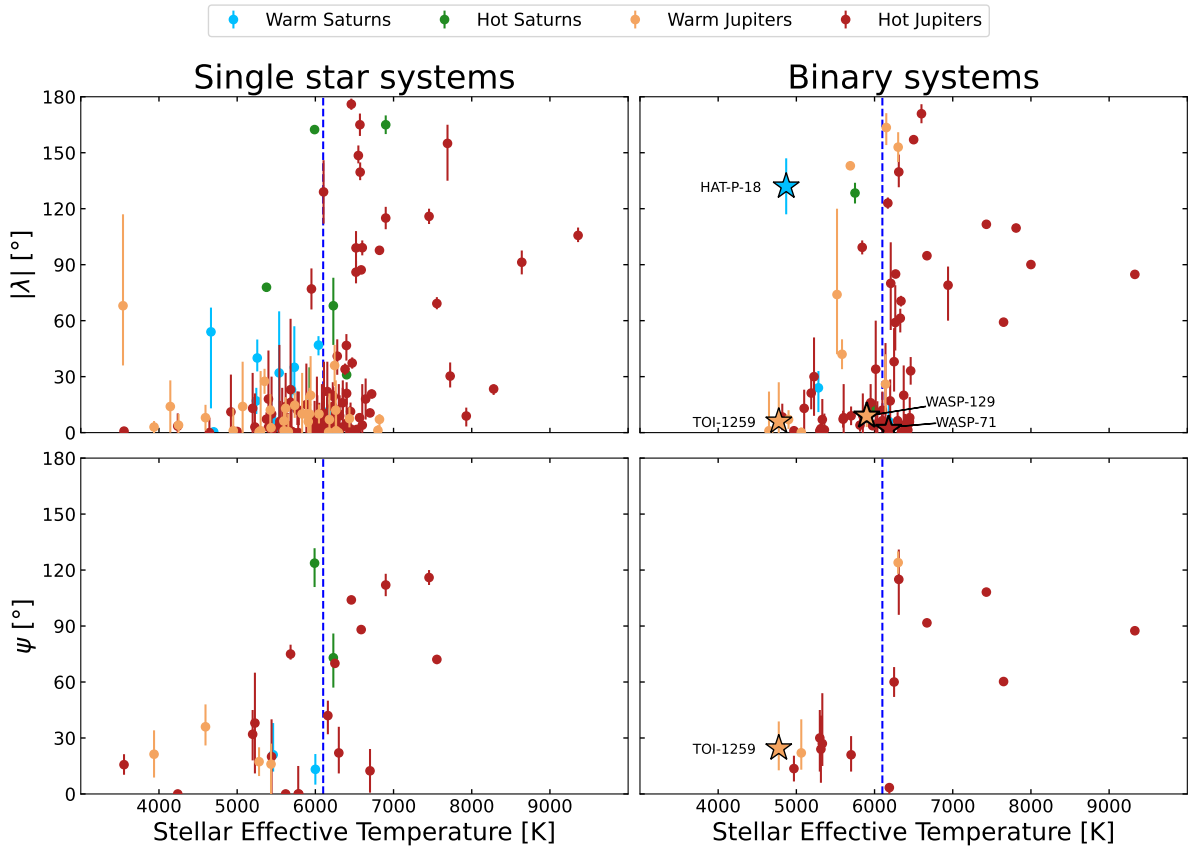

Fig. 3. Sky-projected obliquity λ (upper panels) and 3D obliquity ψ (bottom panels) as a function of the stellar effective temperature for the sample of planets around apparently single stars (left panels) and known binary or triple systems (right panels). Hot Jupiters (defined as having $0.4 < M_p/M_J < 13$ and $a/R_\star < 11$) are shown in red; warm Jupiters ($0.4 < M_p/M_J < 13$ and $a/R_\star > 11$) are shown in orange; hot Saturns ($0.2 < M_p/M_J < 0.4$ and $a/R_\star < 11$) are shown in green; and warm Saturns ($0.2 < M_p/M_J < 0.4$ and $a/R_\star > 11$) are shown in blue. Systems with known binary WD companions are shown as stars. The Kraft break at ~6100 K is shown as a dashed blue line. TOI-1259Ab is only one of the four WD systems with a measured true 3D obliquity.

The picture for warm Jupiters is slightly different. Around single stars, Espinoza-Retamal et al. (2025) shows that all warm Jupiters in their sample are well-aligned (see also, Rice et al. 2022b; Wang et al. 2024). Figure 3 shows the same trend. In binary systems, the warm Jupiters show a wider range of obliquities. The alignment seen in warm Jupiters around single stars is probably a primordial feature, while the higher obliquities around binary stars are more consistent with high-eccentricity migration driven by the stellar companions (e.g., Wu & Murray 2003; Fabrycky & Tremaine 2007). With a WD companion at a projected separation of 1645 au, TOI-1259 (orange star in Figure 3) has a low obliquity compared to a number of other misaligned warm Jupiters in binary systems. Furthermore, TOI-1259Ab is only the third warm Jupiter in a binary system with a true 3D obliquity measurement. As discussed in Section 5.4 below, despite its prograde orbit, TOI-1259Ab remains consistent with formation via ELK migration induced by the WD companion. A planet in a binary system where one of the stars is a WD is relatively rare among a sample of detected planets. Michel & Mugrauer (2024) found 2221 exoplanet-hosting binaries, of which only 17 have a WD companion – ten of which were already compiled by Martin et al. (2021). We find TOI-1259 to be one of four systems containing a known WD companion with a measured stellar obliquity; the other three systems are HAT-P-18 (Esposito et al. 2014), WASP-71 (Smith et al. 2013; Brown et al. 2017), and WASP-129 (Zak et al. 2025). However, the WD companions, HAT-P-18B and WASP-71B, were detected after the obliquity measurements were reported (Mugrauer & Michel 2021; Schlagenhauf et al. 2024; Mugrauer et al. 2022). WASP-129, on the other hand, was found to have a WD companion by Mugrauer & Michel (2021), after which Zak et al. (2025) measured its stellar obliquity. Interestingly, TOI-1259Ab, HAT-P-18Ab, and WASP-129Ab are all warm gas giants but with different obliquities. TOI-1259Ab, WASP-71Ab, and WASP-129Ab are well-aligned with sky-projected obliquities of $\lambda = 6^{+21}_{-22}{}^\circ$, $\lambda = -1.9^{+7.1}_{-7.5}{}^\circ$, and $\lambda = 9 \pm 6^\circ$, respectively. In turn, HAT-P-18Ab is misaligned with a sky-projected obliquity of $\lambda = 132 \pm 15^\circ$.

5.2. Realignment and circularization timescales

To investigate whether the observed properties of these WD systems are a result of primordial or post-formation processes, we began by estimating the timescales for tidal realignment and orbital circularization. Stars that are colder and positioned below the Kraft break have a tidal realignment timescale τ_r that can be estimated as (Zahn 1977; Albrecht et al. 2012)

$$\tau_r = 10 \times 10^9 \left(\frac{M_p}{M_\star}\right)^{-2} \left(\frac{a/R_\star}{40}\right)^6 \text{ yr}. \quad (2)$$

Using the results of the best fit discussed in Section 4, we find a realignment timescale for TOI-1259Ab of $\sim 3 \times 10^4$ Gyr,

which is significantly longer than the age of the universe (e.g., Planck Collaboration VI 2020). This suggests that tides have not significantly affected the obliquity.

To see whether TOI-1259Ab's orbit could have circularized after an eccentric formation process, as in Espinoza-Retamal et al. (2023), we followed Goldreich & Soter (1966) to estimate the tidal circularization timescale:

$$\tau_c \equiv -\frac{e}{\dot{e}} = \frac{2P}{63\pi} Q'_p \left(\frac{M_\mathrm{p}}{M_\star}\right)\left(\frac{a}{R_\mathrm{p}}\right)^5 F(e), \tag{3}$$

where Q'_p is the planet's modified tidal quality factor (Ogilvie & Lin 2007) and $F(e)$ is an eccentricity-dependent correction factor (Hut 1981). Note that P, a, and e correspond to the initial values. Assuming that TOI-1259Ab started migrating with an initial eccentricity $e \sim 0.9$ and pseudo-synchronous rotation of the planet, it yields $F(e) \sim 7 \times 10^{-6}$. Furthermore, assuming $Q'_p = 10^5$–10^6, we estimate $\tau_c = 7$–70 Myr. This means the system could have easily circularized within the age of the system.

To contextualize the tidal timescales of the other three WD-companion systems with an obliquity measurement, we also estimated the values for HAT-P-18, WASP-71, and WASP-129. For HAT-P-18, we find a tidal realignment timescale of $\sim 10^6$ Gyr – too long for realignment to have begun – which is expected for a less massive planet on a relatively wide orbit that does not raise significant tides on its host star (e.g., Louden & Millholland 2024). In turn, its circularization timescale of $\sim 10^2$–10^3 Myr fits easily within the system's age – found by Hartman et al. (2010) to be 12.4 ± 6.4 Gyr. This means it could have undergone high-eccentricity migration driven by the stellar companion and still be observed in a circular and misaligned orbit today.

For WASP-71, the picture is slightly more complicated. Triaud (2011) showed that stars with masses $\geq 1.2\,M_\odot$, such as WASP-71, start on the zero-age main sequence above the Kraft break and are presumably less effective at realigning. But as Smith et al. (2013) noted, WASP-71 could have realigned after the star cooled and developed a convective envelope. However, even when assuming a convective envelope for the star's entire life, we find a realignment timescale of 8.1 Gyr. This is longer than the system's age of ~ 3.5 Gyr reported by Brown et al. (2017). Given its current (nearly) perfect alignment, we argue that WASP-71 has not substantially realigned and formed well-aligned. Circularizing its orbit after eccentric migration would be possible on a much shorter timescale of ~ 12–120 Myr.

Finally, for WASP-129 we estimate a tidal realignment timescale of $\sim 3 \times 10^4$ Gyr and a circularization timescale of ~ 1–10 Gyr – longer than the system's age of ~ 1 Gyr as reported by Maxted et al. (2016). This makes it improbable that WASP-129Ab migrated from an eccentric orbit and suggests a relatively quiescent history.

5.3. γ angle

To shed further light on the possible formation mechanisms of TOI-1259Ab, we followed Rubenzahl et al. (2024) and constrained the angle γ between the vector connecting the astrometric positions of the two stars (**r**) and the difference in sky-projected velocity vectors (**v**) using Gaia DR3 (Gaia Collaboration 2023) positions and proper motions (Figure 4). As discussed by Rubenzahl et al. (2024), any transiting planet has an orbital inclination $i \sim 90°$, and therefore $\gamma \sim 90°$ indicates a large misalignment between the planetary orbit and the binary orbit. On the other hand, observing $\gamma \sim 0°$ or $180°$ is indicative of good alignment, even though the γ angle is also affected by the eccentricity of the binary and the orientation of the line of nodes formed by the intersection of the planetary orbital plane and the sky plane.

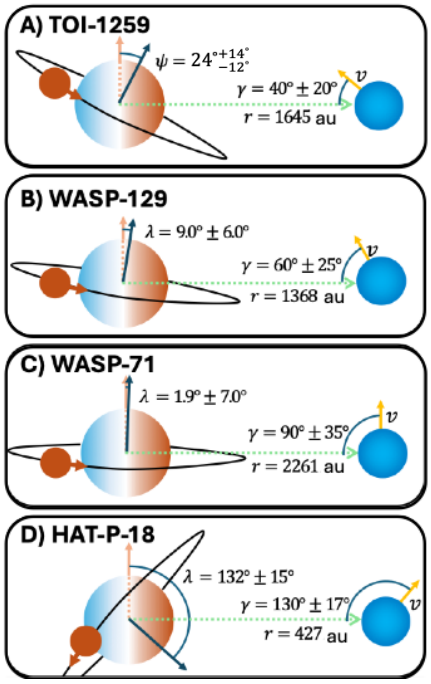

Fig. 4. Diagram depicting the relative angles of the WD binary systems. The obliquity ψ (or λ when only the sky-projected obliquity is known) and γ angle – defined between the vector connecting the astrometric positions of the two stars (**r**) and the difference in velocity vectors (**v**) – found in this study are shown, along with the sky-projected separations. The γ angle is affected by the eccentricity, and its relation to the orientation of the planet's orbit is unknown; thus, the γ angle alone cannot constrain the orbits and is merely a proxy measurement. Distances and sizes are not to scale.

Following the formalism from Hwang et al. (2022), for TOI-1259 we derive $\gamma = 40 \pm 20°$. Even with high uncertainties in γ, the biggest barrier to identifying whether the binary orbit is aligned or misaligned with the planetary orbit are the unknown longitude of nodes in the system. As such, we argue – and further show in Section 5.4 – that the ELK mechanism has room to operate, as the WD companion is a potentially inclined perturber capable of driving the cycles that cause the planet to migrate.

In the other three WD systems, the ELK mechanism has even more room to operate. The HAT-P-18 system has $\gamma = 130 \pm 15°$ (Rice et al. 2024); we estimate $\gamma = 90 \pm 35°$ for WASP-71 and find $\gamma = 60 \pm 25°$ for WASP-129. In all cases, the binary and planetary orbits are highly misaligned, suggesting that the WD companion may be in a favorable configuration for driving ELK cycles. All system configurations are shown in Figure 4.

5.4. Formation pathways

With TOI-1259Ab being on a low-obliquity or slightly misaligned orbit without the ability to tidally realign, many mechanisms could explain its obliquity. Given this, decisively tracing the system's obliquity to primordial or post-formation misalignment – or both – is difficult. We briefly comment on these possibilities below.

Primordial alignment: the low-obliquity orbit of TOI-1259Ab could be a relic of a primordial alignment between the

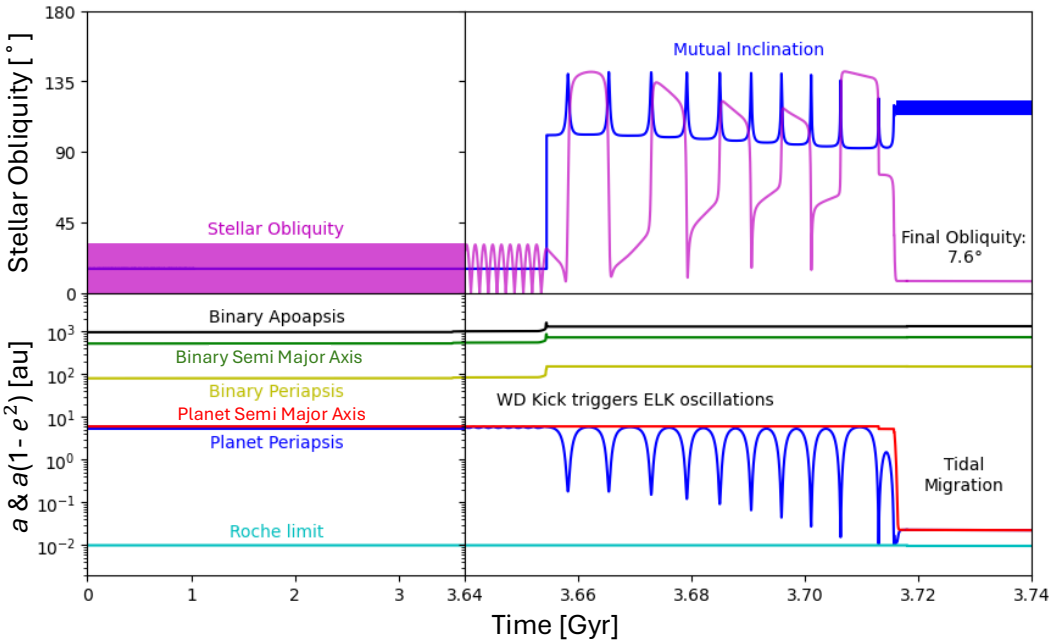

Fig. 5. Example evolution of a well-aligned gas giant in a binary system consistent with the TOI-1259 system. In this system, ELK oscillations are initially absent due to the low mutual inclination between the planetary and binary orbits (upper panels, blue line). The stellar obliquity (upper panels, magenta line) initially oscillates due to precession of the planetary orbit's line of nodes around the total system angular momentum. However, the WD kick changes the orbital parameters of the system and triggers strong ELK oscillations (lower right panel), causing high eccentricities for the planetary orbit and short periapsis distances (lower panels, blue line) and eventually leading to shrinking of the planet's semimajor axis (lower panels, red line) via tidal migration. In this simulation, the planet's final obliquity is 7.6°, and the final mutual inclination between the planetary and binary orbits is high (and oscillatory, as the planetary orbit normal precesses around the star's spin axis due to tidal coupling). The WD companion has a wide final orbit with an apoapsis distance (lower panels, black line) of about 1300 au, consistent with the projected separation of the TOI-1259 binary.

star and the protoplanetary disk in which the planet formed and possibly underwent disk migration to arrive at the configuration we currently observe (e.g., Goldreich & Tremaine 1980; Lin & Papaloizou 1986; Ward 1997). The small degree of misalignment compatible with the data could have been produced either by tilting the disk due to gravitational torques from the binary stellar companion TOI-1259B (e.g., Batygin 2012; Lai 2014; Zanazzi & Lai 2018) or by a magnetic torque between the inner disk and the host star. This could have given the star a slight inclination with respect to the initial planet-forming disk (Lai et al. 2011).

Post formation: a system such as TOI-1259 could also form through high-eccentricity migration, and more specifically through the WD kick formation scenario presented by Stephan et al. (2024). In this scenario, giant planets form in wide orbits, experience ELK oscillations, and eventually undergo high-eccentricity migration after the WD kick tilts the WD's orbit away from the planet's orbital plane. The systems we observe – except WASP-129 – have circularization timescales shorter than their ages, making this pathway plausible. With the WD and planet on inclined orbits, this could lead to a broad range of values for the resulting stellar obliquity. In the observed sample, HAT-P-18 shows misalignment, while TOI-1259 and WASP-71 are consistent with good alignment. As discussed further below, the outcomes of the ELK oscillations can result in a broad array of obliquities, suggesting that all the systems would be compatible with the WD kick formation scenario. Indeed, Saidel et al. (2025) also concluded that if TOI-1259Ab formed far out, ELK migration induced by the WD companion would be a plausible migration pathway. This follows from the timescale of ELK oscillations being shorter than that of the pericenter precession.

5.5. Dynamical simulation of the ELK scenario

To gauge how consistent the WD kick formation scenario is with our observation of good alignment for TOI-1259Ab, we conducted dynamical simulations of 10 000 systems using the code of Stephan et al. (2024), with the simulation parameters tailored to the TOI-1259 system (see Fig. 5 for an example simulation that produces a system consistent with TOI-1259). For the simulation, we set the primary star's mass to 0.744 $M_\odot$ and the planet's mass and radius to 0.441 M_J and 1.022 R_J, respectively. The stellar companion's initial mass was chosen randomly between 1.4 and 1.6 $M_\odot$, such that it would evolve into an approximately 0.57 $M_\odot$ WD consistent with observations of TOI-1259B (Fitzmaurice et al. 2022), as determined by the stellar evolution code SSE (Hurley et al. 2000). The planet's orbit was set to be initially circular, with an initial semimajor axis (a) chosen randomly between 1 and 10 au and aligned with the primary star's spin. The companion star's orbit initially had a random eccentricity between 0 and 1, with an initial semimajor axis chosen randomly between 10 and 10 000 au, following a log-Gaussian distribution as described by Duquennoy & Mayor (1991). The inclination between the two orbits was chosen randomly following an isotropic distribution (uniform in cosine), and the arguments of periapsis were chosen randomly between 0 and 360°. Only configurations that are long-term stable and hierarchical enough for EKL to be relevant were chosen for the simulations (see, e.g., Naoz 2016). Finally, the WD formation kick followed the empirically determined kick parameters from El-Badry & Rix (2018). The kick velocity was drawn from a Maxwellian distribution, with the typical kick velocity (peak of the distribution) being about 0.75 km s^{-1}. As we were agnostic

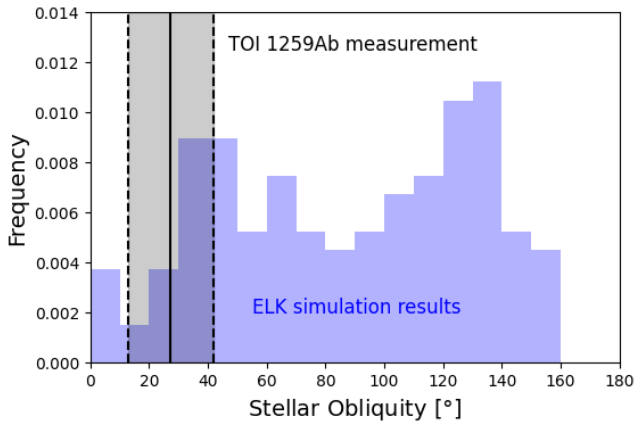

Fig. 6. Distribution of stellar obliquities for hot and warm Jupiters from our ELK simulations (blue histogram), compared to the measured obliquity of TOI 1259Ab including 1σ uncertainties (gray-shaded region). About 14% of the simulated close-in Jupiter systems have final obliquities consistent with the measured obliquity (19% if any systems with obliquities lower than our measurement are included).

about the exact kick mechanism during WD formation, the kick direction was chosen randomly.

Our main interest in these simulations is in the obliquity distribution of the resulting hot and warm Jupiters formed. While it is generally expected that ELK produces mostly misaligned planets, previous studies have shown that a nonzero fraction of systems produce nearly aligned systems (e.g., Naoz et al. 2012). As the formation pathway of Stephan et al. (2024) does include a WD kick, we chose to conduct new simulations to specifically test how likely it is for ELK with kicks to produce systems consistent with our observations for TOI-1259. The resulting population, seen in Figure 6, is a combination of pre- and post-kick migration with a roughly even split and similar ψ distributions. We find that, indeed, about 14% of our simulations produce final obliquities consistent with the measured obliquity for TOI 1259Ab. If we also include any systems with obliquities lower than our measurement, this number rises to 19%. These results indicate that the ELK mechanism with WD kicks efficiently produces short-period gas giants with low obliquities.

6. Conclusions

Using in-transit RV observations with the NEID spectrograph, we have demonstrated that TOI-1259Ab – a warm Jupiter orbiting a K star with a WD companion – has a low-obliquity orbit with a sky-projected obliquity of $\lambda = \mathbf{7}^{+\mathbf{20}^\circ}_{-\mathbf{21}}$. Combining the sky-projected obliquity constraint from the RM analysis with the stellar rotation period and the stellar radius yields a true 3D obliquity of $\psi = 24^{+14^\circ}_{-12}$, compatible with a prograde orbit. We simulated 10 000 WD kick-induced evolutions of systems such as TOI-1259, which resulted in obliquities consistent with our observations in 14 % of the systems, making it a plausible formation pathway. However, for TOI-1259Ab, we cannot rule out more quiescent formation via, for example, disk-driven migration. Along with HAT-P-18, WASP-71, and WASP-129, TOI-1259 is the fourth system with a WD companion whose obliquity is measured – beginning to form a new population for studying the influence of stellar evolution on the dynamical evolution of planetary systems.

Data availability

A reproduction package can be found on Zenodo https://zenodo.org/records/17361032. The package includes the RV data from NEID and SOPHIE and the TESS transit data alongside the scripts used to model this data using `ironman`. It also includes Jupyter notebooks to produce the population plot shown in Figure 3.

Acknowledgements. We thank the Red Worlds Lab research group at the University of Amsterdam for their thoughtful discussions and suggestions that strengthened the manuscript. J.I.E.-R. gratefully acknowledges support from the John and A-Lan Reynolds Faculty Research Fund, from ANID BASAL project FB210003, and from ANID Doctorado Nacional grant 2021-21212378. We thank the NEID Queue Observers and WIYN Observing Associates for their skillful execution of our observations. Data presented were obtained by the NEID spectrograph built by Penn State University and operated at the WIYN Observatory by NOIRLab, under the NN-EXPLORE partnership of the National Aeronautics and Space Administration and the National Science Foundation. The NEID archive is operated by the NASA Exoplanet Science Institute at the California Institute of Technology. Based in part on observations at the Kitt Peak National Observatory (Prop. ID 2022A-970114), managed by the Association of Universities for Research in Astronomy (AURA) under a cooperative agreement with the National Science Foundation. The WIYN Observatory is a joint facility of the NSF's National Optical-Infrared Astronomy Research Laboratory, Indiana University, the University of Wisconsin-Madison, Pennsylvania State University, Purdue University, and Princeton University. The authors are honored to be permitted to conduct astronomical research on Iolkam Du'ag (Kitt Peak), a mountain with particular significance to the Tohono O'odham. Data presented herein were obtained from telescope time allocated to NN-EXPLORE through the scientific partnership of the National Aeronautics and Space Administration, the National Science Foundation, and the National Optical Astronomy Observatory. The research was carried out at the Jet Propulsion Laboratory, California Institute of Technology, under a contract with the National Aeronautics and Space Administration (80NM0018D0004). This work was partially supported by funding from the Center for Exoplanets and Habitable Worlds. The Center for Exoplanets and Habitable Worlds is supported by the Pennsylvania State University, the Eberly College of Science, and the Pennsylvania Space Grant Consortium. Computations for this research were performed on the Pennsylvania State University's Institute for Computational & Data Sciences (ICDS). This work has made use of data from the European Space Agency (ESA) mission Gaia processed by the Gaia Data Processing and Analysis Consortium (DPAC). Funding for the DPAC has been provided by national institutions, in particular the institutions participating in the Gaia Multilateral Agreement. This research made use of the NASA Exoplanet Archive, which is operated by the California Institute of Technology, under contract with the National Aeronautics and Space Administration under the Exoplanet Exploration Program. This work used computational and storage services associated with the Hoffman2 Shared Cluster provided by UCLA Office of Advanced Research Computing's Research Technology Group, and the resources provided by the Vanderbilt Advanced Computing Center for Research and Education (ACCRE).

References

Aguilera-Gómez, C., Rogers, L. K., Bonsor, A., et al. 2025, A&A, 693, A64
Akeson, R., Chen, X., Ciardi, D., et al. 2013, PASP, 125, 989
Albrecht, S., Winn, J. N., Johnson, J. A., et al. 2012, ApJ, 757, 18
Albrecht, S. H., Marcussen, M. L., Winn, J. N., Dawson, R. I., & Knudstrup, E. 2021, ApJ, 916, L1
Albrecht, S. H., Dawson, R. I., & Winn, J. N. 2022, PASP, 134, 082001
Attia, M., Bourrier, V., Delisle, J.-B., & Eggenberger, P. 2023, A&A, 674, A120
Batygin, K. 2012, Nature, 491, 418
Batygin, K., Bodenheimer, P. H., & Laughlin, G. P. 2016, ApJ, 829, 114
Beaugé, C., & Nesvorný, D. 2012, ApJ, 751, 119
Beck, J. G., & Giles, P. 2005, ApJ, 621, L153
Boley, A. C., Granados Contreras, A. P., & Gladman, B. 2016, ApJ, 817, L17
Bourrier, V., Attia, M., Mallonn, M., et al. 2023, A&A, 669, A63
Brown, D., Triaud, A., Doyle, A., et al. 2017, MNRAS, 464, 810
Christiansen, J. L., McElroy, D. L., Harbut, M., et al. 2025, arXiv preprint [arXiv:2506.03299]
Dawson, R. I., & Johnson, J. A. 2018, ARA&A, 56, 175
Dong, J., & Foreman-Mackey, D. 2023, AJ, 166, 112
Duquennoy, A., & Mayor, M. 1991, A&A, 248, 485

El-Badry, K., & Rix, H.-W. 2018, MNRAS, 480, 4884
El-Badry, K., Rix, H.-W., & Heintz, T. M. 2021, MNRAS, 506, 2269
Espinoza, N., Kossakowski, D., & Brahm, R. 2019, MNRAS, 490, 2262
Espinoza-Retamal, J. I., Brahm, R., Petrovich, C., et al. 2023, ApJ, 958, L20
Espinoza-Retamal, J. I., Stefánsson, G., Petrovich, C., et al. 2024, AJ, 168, 185
Espinoza-Retamal, J. I., Jordán, A., Brahm, R., et al. 2025 [arXiv:2412.08692]
Esposito, M., Covino, E., Mancini, L., et al. 2014, A&A, 564, L13
Fabrycky, D., & Tremaine, S. 2007, ApJ, 669, 1298
Fitzmaurice, E., Martin, D. V., Rodríguez Martínez, R., et al. 2022, MNRAS, 518, 636
Foreman-Mackey, D., Agol, E., Angus, R., & Ambikasaran, S. 2017, AJ, 154, 220
Fregeau, J. M., Richer, H. B., Rasio, F. A., & Hurley, J. R. 2009, ApJ, 695, L20
Fulton, B. J., Petigura, E. A., Blunt, S., & Sinukoff, E. 2018, PASP, 130, 044504
Gaia Collaboration (Vallenari, A., et al.) 2023, A&A, 674, A1
Goldreich, P., & Soter, S. 1966, Icarus, 5, 375
Goldreich, P., & Tremaine, S. 1980, ApJ, 241, 425
Hartman, J., Bakos, G., Sato, B., et al. 2010, ApJ, 726, 52
Hedges, C., Angus, R., Barentsen, G., et al. 2020, RNAAS, 4, 220
Hirano, T., Suto, Y., Taruya, A., et al. 2010, AJ, 709, 458
Hurley, J. R., Pols, O. R., & Tout, C. A. 2000, MNRAS, 315, 543
Hut, P. 1981, A&A, 99, 126
Hwang, H.-C., Ting, Y.-S., & Zakamska, N. L. 2022, MNRAS, 512, 3383
Jenkins, J. M., Twicken, J. D., McCauliff, S., et al. 2016, SPIE Conf. Ser., 9913, 99133E
Knudstrup, E., Albrecht, S. H., Winn, J. N., et al. 2024, A&A, 690, A379
Koester, D., Gänsicke, B. T., & Farihi, J. 2014, A&A, 566, A34
Kozai, Y. 1962, AJ, 67, 591
Kraft, R. P. 1967, ApJ, 150, 551
Kraus, S., Le Bouquin, J.-B., Kreplin, A., et al. 2020, ApJ, 897, L8
Kreidberg, L. 2015, PASP, 127, 1161
Lai, D. 2014, MNRAS, 440, 3532
Lai, D., Foucart, F., & Lin, D. N. 2011, MNRAS, 412, 2790
Lidov, M. L. 1962, Planet. Space Sci., 9, 719
Lightkurve Collaboration (Cardoso, J. V. d. M., et al.) 2018, Lightkurve: Kepler and TESS time series analysis in Python, Astrophysics Source Code Library
Lin, D. N. C., & Papaloizou, J. 1986, ApJ, 309, 846
Louden, E. M., & Millholland, S. C. 2024, ApJ, 974, 304
Martin, D. V., El-Badry, K., Hodžić, V. K., et al. 2021, MNRAS, 507, 4132
Martínez, R. R., Gaudi, B. S., Rodriguez, J. E., et al. 2020, ApJ, 160, 111
Masuda, K., & Winn, J. N. 2020, AJ, 159, 81
Maxted, P., Anderson, D., Cameron, A. C., et al. 2016, A&A, 591, A55
Mayor, M., & Queloz, D. 1995, Nature, 378, 355
McLaughlin, D. 1924, ApJ, 60, 22
Michel, K.-U., & Mugrauer, M. 2024, MNRAS, 527, 3183
Mugrauer, M., & Michel, K.-U. 2021, Astron. Nachr., 342, 840
Mugrauer, M., Zander, J., & Michel, K.-U. 2022, Astron. Nachr., 343, e20224017
Naoz, S. 2016, ARA&A, 54, 441
Naoz, S., Farr, W. M., & Rasio, F. A. 2012, ApJ, 754, L36
Ogilvie, G. I., & Lin, D. N. C. 2007, ApJ, 661, 1180
Perruchot, S., Kohler, D., Bouchy, F., et al. 2008, in Ground-based and Airborne Instrumentation for Astronomy II, 7014, SPIE, 235
Petrovich, C. 2015, ApJ, 805, 75
Planck Collaboration VI. 2020, A&A, 641, A6
Rasio, F. A., & Ford, E. B. 1996, Science, 274, 954
Rice, M., Wang, S., & Laughlin, G. 2022a, ApJ, 926, L17
Rice, M., Wang, S., Wang, X.-Y., et al. 2022b, AJ, 164, 104
Rice, M., Gerbig, K., & Vanderburg, A. 2024, AJ, 167, 126
Ricker, G. R., Winn, J. N., Vanderspek, R., et al. 2015, J. Astron. Telesc. Instrum. Syst., 1, 014003
Robertson, P., Anderson, T., Stefansson, G., et al. 2019, J. Astron. Telesc. Instrum. Syst., 5, 015003
Rossiter, R. 1924, ApJ, 60, 15
Rubenzahl, R. A., Dai, F., Halverson, S., et al. 2024, AJ, 168, 188
Saidel, M., Vissapragada, S., Spake, J., et al. 2025, ApJ, 169, 104
Saumon, D., Blouin, S., & Tremblay, P.-E. 2022, Phys. Rep., 988, 1
Schlagenhauf, S., Mugrauer, M., Ginski, C., et al. 2024, MNRAS, 529, 4768
Schlaufman, K. C. 2010, ApJ, 719, 602
Schwab, C., Rakich, A., Gong, Q., et al. 2016, in Ground-based and Airborne Instrumentation for Astronomy VI, 9908, SPIE, 2220
Siegel, J. C., Winn, J. N., & Albrecht, S. H. 2023, ApJ, 950, L2
Smith, A., Anderson, D., Bouchy, F., et al. 2013, A&A, 552, A120
Southworth, J. 2011, MNRAS, 417, 2166
Speagle, J. S. 2020, MNRAS, 493, 3132
Stefansson, G., Hearty, F., Robertson, P., et al. 2016, ApJ, 833, 175
Stefànsson, G., Mahadevan, S., Maney, M., et al. 2020, AJ, 160, 192
Stefànsson, G., Mahadevan, S., Petrovich, C., et al. 2022, ApJ, 931, L15
Stephan, A. P., Martin, D. V., Naoz, S., Hughes, N. R., & Shariat, C. 2024, ApJ, 977, L11
Triaud, A. H. 2011, A&A, 534, L6
Valenti, J. A., & Fischer, D. A. 2005, ApJS, 159, 141
Vanderburg, A., Rappaport, S. A., Xu, S., et al. 2020, Nature, 585, 363
Ward, W. R. 1997, Icarus, 126, 261
Wang, X.-Y., Rice, M., Wang, S., et al. 2024, arXiv e-prints [arXiv:2408.10038]
Winn, J. N., Fabrycky, D., Albrecht, S., & Johnson, J. A. 2010, ApJ, 718, L145
Wu, Y., & Murray, N. 2003, ApJ, 589, 605
Wu, Y., & Lithwick, Y. 2011, ApJ, 735, 109
Zahn, J.-P. 1977, A&A, 57, 383
Zak, J., Boffin, H., Bocchieri, A., et al. 2025, arXiv preprint [arXiv:2505.20516]
Zanazzi, J. J., & Lai, D. 2018, MNRAS, 478, 835
Zanazzi, J. J., Dewberry, J., & Chiang, E. 2024, ApJ, 967, L29
Zechmeister, M., Reiners, A., Amado, P. J., et al. 2018, A&A, 609, A12
Zhao, L. L., Kunovac, V., Brewer, J. M., et al. 2023, Nat. Astron., 7, 198
Zuckerman, B. 2014, ApJ, 791, L27
Zuckerman, B., Melis, C., Klein, B., Koester, D., & Jura, M. 2010, ApJ, 722, 725

Appendix A: NEID radial velocities

Table A.1. NEID RV measurements of TOI-1259A.

BJD	Radial Velocity (m s^{-1})	Radial Velocity Uncertainty (m s^{-1})
2459691.743419	0.8	6.9
2459691.750682	-3.6	6.9
2459691.768026	5.3	8.1
2459691.775289	19.8	7.4
2459691.782554	0.3	6.2
2459691.789818	-2.2	5.8
2459691.797083	13.1	6.6
2459691.804348	23.8	8.2
2459691.811613	28.1	9.5
2459691.818877	19.1	7.5
2459691.826142	14.8	7.2
2459691.833407	-2.1	7.4
2459691.840671	-4.6	7.7
2459691.847936	-30.6	9.4
2459691.855201	-32.5	9.5
2459691.862466	-33.1	8.6
2459691.869730	-34.8	7.3
2459691.876995	-22.3	8.0
2459691.884260	15.6	8.8
2459691.891524	-13.6	8.6
2459691.898789	2.8	7.4
2459691.906054	-8.3	5.6
2459691.913319	-16.8	8.5
2459691.920583	4.6	10.0
2459691.927848	-19.1	9.6
2459691.935113	1.6	7.9

Appendix B: Posterior distributions

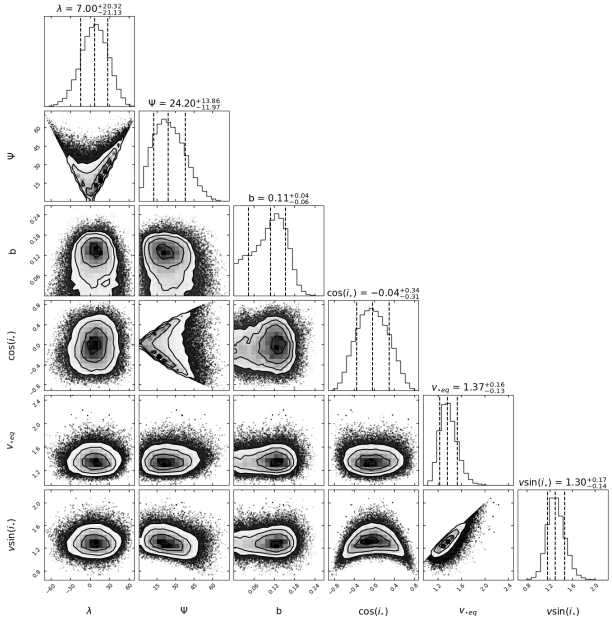

Table B.1. Posterior distributions of select parameters from Table 1. Joint posterior distributions and histograms of some of the posteriors from the joint ironman fit.